



Direct measurement of lipid membrane disruption connects kinetics and toxicity of A β 42 aggregation

Patrick Flagmeier^{1,7}, Suman De^{1,7}, Thomas C. T. Michaels^{1,2,7}, Xiaoting Yang¹, Alexander J. Dear^{1,2}, Cecilia Emanuelsson³, Michele Vendruscolo¹, Sara Linse³, David Klenerman^{4,5}✉, Tuomas P. J. Knowles^{1,6}✉ and Christopher M. Dobson¹

The formation of amyloid deposits in human tissues is a defining feature of more than 50 medical disorders, including Alzheimer's disease. Strong genetic and histological evidence links these conditions to the process of protein aggregation, yet it has remained challenging to identify a definitive connection between aggregation and pathogenicity. Using time-resolved fluorescence microscopy of individual synthetic vesicles, we show for the A β 42 peptide implicated in Alzheimer's disease that the disruption of lipid bilayers correlates linearly with the time course of the levels of transient oligomers generated through secondary nucleation. These findings indicate a specific role of oligomers generated through the catalytic action of fibrillar species during the protein aggregation process in driving deleterious biological function and establish a direct causative connection between amyloid formation and its pathological effects.

Neurodegenerative conditions including Alzheimer's and Parkinson's diseases^{1–5} have emerged as main challenges to the health and social systems of the modern world as a result of their increasing prevalence in our aging populations. A substantial body of data indicates that protein aggregation is a key factor underlying these disorders^{6–14}. Recent progress in understanding the molecular mechanisms of aggregation has revealed that these processes typically involve a primary nucleation step, followed by the growth of the initial aggregates through an elongation process (Fig. 1a)^{15–18}. Once a critical quantity of fibrils is formed, however, the aggregation reaction can be accelerated dramatically by secondary processes in which fibrils formed during the aggregation reaction promote the formation of further aggregates (Fig. 1a)^{17,18}. A prominent example of such secondary processes is surface-catalyzed secondary nucleation, which is particularly significant for the A β peptides associated with Alzheimer's disease, and has been linked to a variety of mechanisms of neuronal damage^{4,5,17,18}. Indeed, the disruption of the lipid bilayer in cellular membranes by oligomeric protein aggregates, and the consequent loss of Ca²⁺ homeostasis, has been proposed as a general mechanism of neurotoxicity^{19–21}.

In the context of Alzheimer's disease, a key objective is to connect the time dependence of lipid bilayer permeability to that of the aggregation reaction and to the resulting distribution of aggregated forms of A β 42, the 42-residue A β peptide that has been most strongly linked to neurological damage. Such data would serve to establish the species and processes associated with an ongoing A β 42 aggregation reaction that are primarily responsible for causing lipid bilayer permeability. This information would be particularly useful for elucidating the mechanisms of pathological protein aggregation, which still remain poorly understood, a possible reason for the

heterogeneous outcome of clinical trials aimed at targeting amyloid formation^{22–24}.

To address this question, we have combined recent advances in the mechanistic analysis of experimental measurements of protein aggregation kinetics in vitro^{15,25} with the development of a single molecule optochemical approach able to quantify the degree of membrane permeability resulting from the aggregation reaction at any point in time²⁶. Using this platform, we reveal the dominant role of transient A β 42 oligomers generated by secondary nucleation²⁷ in driving membrane permeation.

Results

Link between aggregation of A β 42 and lipid bilayer permeability.

We first monitored the extent of membrane disruption by measuring the time dependence of the permeability of the lipid bilayers of synthetic vesicles when monomeric A β 42 was incubated at concentrations between 2 and 4 μ M under solution conditions where the kinetics of amyloid fibril formation have been shown to be highly reproducible²⁸ (Extended Data Fig. 1 and Methods). We also added 2.5% molar monomer equivalents of preformed A β 42 fibrils (seeds) to a solution of 2 μ M monomeric A β 42 (Methods). Addition of such seed fibrils accelerates the aggregation reaction by bypassing the primary nucleation step, providing a convenient and robust way to disentangle secondary nucleation from primary nucleation^{17,18}. In each case, at specific time points, aliquots were removed from the aggregating solutions, added to lipid vesicles, and the extent of Ca²⁺ influx measured using the optochemical method²⁶. We found that the ability of the aggregation reaction mixture to induce bilayer permeability increased with time, reaching a maximum value in the growth phase that is clearly observable in bulk measurements, and

¹Centre for Misfolding Diseases, Department of Chemistry, University of Cambridge, Cambridge, UK. ²Paulson School of Engineering and Applied Science, Harvard University, Cambridge, MA, USA. ³Department of Chemistry, Division for Biochemistry and Structural Biology, Lund University, Lund, Sweden.

⁴Department of Chemistry, University of Cambridge, Cambridge, UK. ⁵UK Dementia Research Institute, University of Cambridge, Cambridge, UK.

⁶Cavendish Laboratory, University of Cambridge, Cambridge, UK. ⁷These authors contributed equally: Patrick Flagmeier, Suman De, Thomas C. T. Michaels.

✉e-mail: dk10012@cam.ac.uk; tpjk2@cam.ac.uk

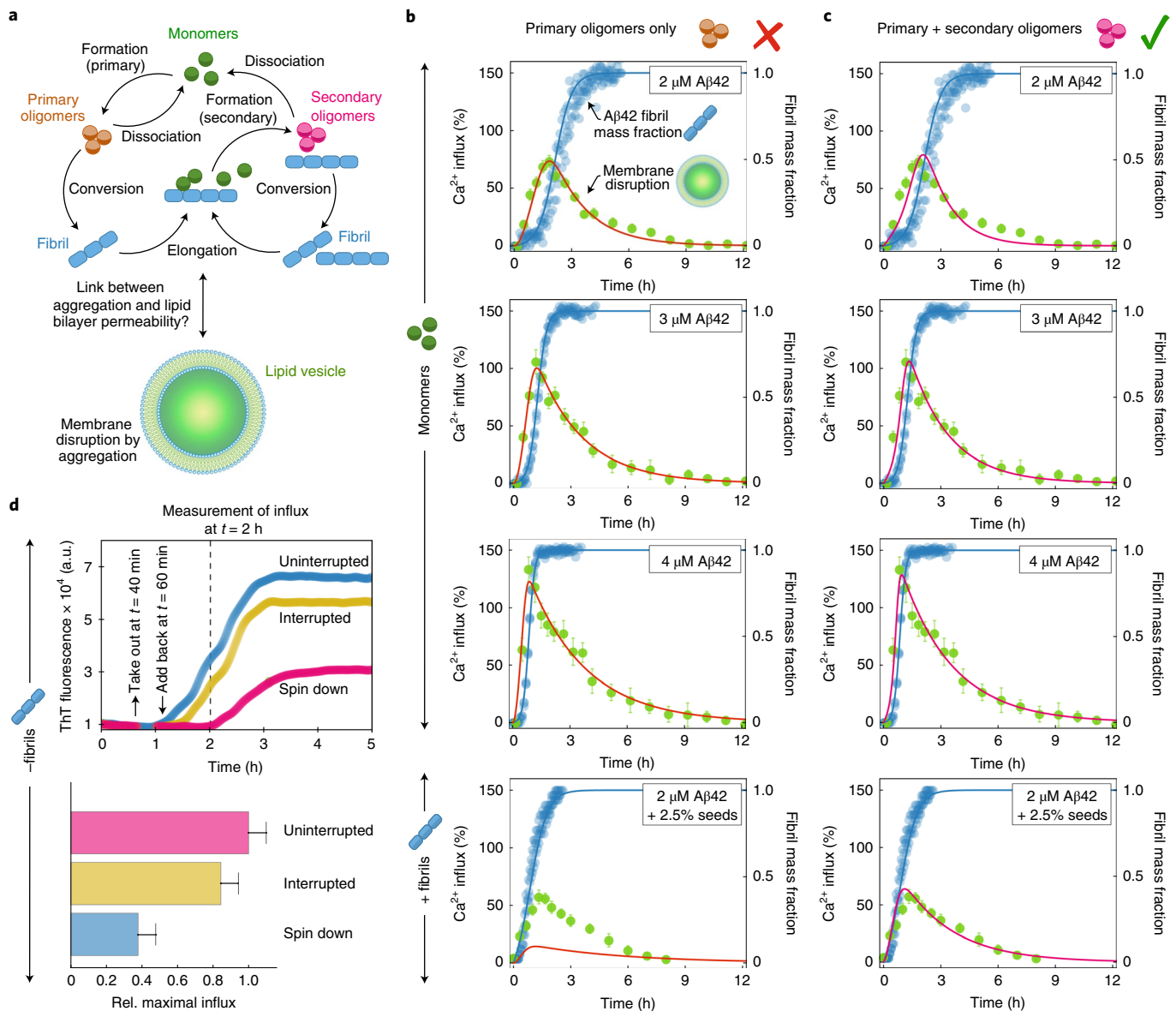


Fig. 1 | Link between aggregation of A β 42 and lipid bilayer permeability. Secondary nucleation generates the oligomers that are associated with the lipid bilayer permeation induced by A β 42 aggregation. **a**, Schematic illustration of the network of molecular steps involved in A β 42 aggregation and the oligomeric species with the potential to cause lipid bilayer permeability (see Supplementary Note 1 for details)^{17,27}. **b,c**, Kinetic analysis of the time evolution of the extent of Ca $^{2+}$ influx during A β 42 aggregation when monomeric A β 42 was incubated under quiescent conditions at concentrations of 2 μ M (first row), 3 μ M (second row), 4 μ M (third row) and 2 μ M in the presence of 2.5% preformed seed fibrils (fourth row). **b**, Best fit of experimental Ca $^{2+}$ -influx data to a kinetic model that assumes only oligomers generated by primary nucleation to be responsible for lipid bilayer permeation (Supplementary Note 1, equation (7), solid lines). Coefficient of determination for global fits $R^2 = 0.91$. **c**, Best fit of the same experimental data to a kinetic model that assumes oligomers generated through secondary nucleation to be responsible for Ca $^{2+}$ influx (Supplementary Note 1, equation (8), solid lines). The various measurements of Ca $^{2+}$ influx at different concentrations of A β 42 and in the presence of preformed fibrils are consistent with a kinetic model where secondary nucleation generates most oligomers that cause lipid bilayer permeability. The fitting parameters, the derivation of the equations and a detailed description of the analysis can be found in the Supplementary Note 1 and Supplementary Tables 1 and 2. **d**, Fibril spin-down experiment. An aggregation reaction starting with 2 μ M monomeric A β 42 was taken out at 40 min and put back at 60 min following centrifugation to remove fibrils or without centrifugation. The bar charts show the measured for the extent of Ca $^{2+}$ influx at 2 h. Error bars indicate s.e.m. over three experiments with independent samples. a.u., arbitrary units.

then slowly decreased during the remainder of the aggregation reaction (Fig. 1b,c).

Since membrane permeation is directly linked in our assay to the aggregation process, we used a chemical kinetics approach to describe the time evolution of Ca $^{2+}$ influx, $\Phi(t)$, in terms of the concentrations $c(t)$ at time t of different types of aggregate species

that could give rise to membrane permeability¹⁶ (Fig. 1a and Supplementary Note 1). In particular, due to the transient nature of Ca $^{2+}$ influx, these aggregate species include intermediate oligomers generated either by primary nucleation (primary oligomers) or by secondary nucleation (secondary oligomers)²⁷. We used the law of mass action to represent Ca $^{2+}$ influx very generally as a power-law

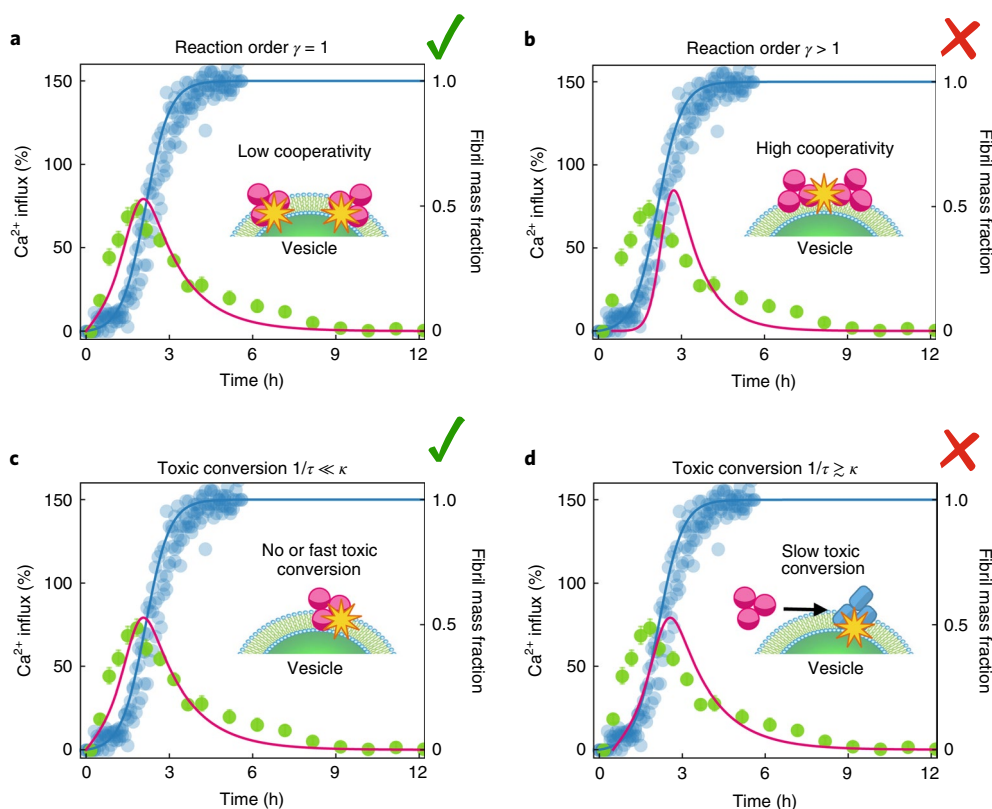


Fig. 2 | Role of oligomer cooperativity and structural reorganization. **a, b**, Best fit of experimental Ca^{2+} -influx data to a secondary oligomer kinetic model with reaction order $\gamma = 1$ (low oligomer cooperativity, **a**) and $\gamma > 1$ (high oligomer cooperativity, **b**); fit shown here for $\gamma = 3$, see Extended Data Fig. 4a). **c, d**, Analysis of membrane permeation measurements using a kinetic model that assumes that oligomers generated initially through secondary nucleation are not damaging on their formation, but are required to convert into species that are able to induce bilayer permeation. The theoretical predictions were generated assuming either fast ($1/\tau \ll \kappa$, **c**) or slow ($1/\tau \gtrsim \kappa$, **d**; see Extended Data Fig. 4b) rate of toxic conversion as compared to the characteristic proliferation rate of the aggregation reaction (κ)¹⁶. This analysis shows that, to describe the membrane permeation data, it is not necessary to invoke a slow conversion step of oligomers into species that are able to induce bilayer permeation. If such a conversion step exists, it must occur on a timescale that is faster than that of the overall aggregation process. Error bars indicate s.e.m. over three experiments with independent samples.

of the concentration of oligomers, $\Phi(t) \propto c(t)^\gamma$, where $\gamma \geq 1$ is the reaction order of membrane permeation with respect to the concentration of oligomers (Supplementary Note 1). γ is a measure of the cooperativity between oligomers in causing membrane permeation. We then described the time evolution of the concentrations of primary and secondary oligomers during aggregation using a master equation (Supplementary Note 1, equation (1)). Using approaches drawing on self-consistent theory^{16,27}, we derived explicit mathematical expressions for the time course of fibril formation and for the concentrations of oligomers in these two specific mechanistic scenarios (Supplementary Note 1), and then compared each of them to the experimental data describing the extent of Ca^{2+} influx over time (Fig. 1b,c). Specifically, we first fitted globally the different kinetic traces of amyloid fibril formation to our kinetic model (Supplementary Note 1, equation (2)) to determine combined rate parameters associated with primary and secondary nucleation (Supplementary Table 1). These parameters were then implemented in the theoretical oligomer concentration curves (Supplementary Note 1, equations (5) and (6)), leaving the combined rates of oligomer dissociation and conversion, the proportionality constant between oligomer concentrations and the extent of Ca^{2+} influx, and the reaction order γ as fitting parameters (Supplementary Table 2 and Supplementary Note 1).

This global analysis reveals that the membrane permeation data are well described by a scenario in which most of the species causing lipid bilayer permeability is generated by secondary nucleation

(Fig. 1c) but not by primary nucleation (Fig. 1b). Note that the former scenario (Fig. 1c) explicitly considers contributions from both primary and secondary oligomers (Supplementary Note 1, equation (8)), even though the primary oligomers are a substantial proportion of the oligomer population only during the initial stages but are otherwise outnumbered by secondary oligomers for the rest of the reaction (Extended Data Fig. 2). We also note that in comparing the different mechanistic scenarios, we consider fit quality globally across a variety of conditions (concentration, seeds), since fits to individual kinetic traces are insufficient to accept or reject a particular mechanism¹⁶. In particular, the inability of the primary oligomer model to describe the membrane permeation data stems from the fact that the primary nucleation pathway for A β 42 is negligible in the presence of preformed fibrils (Extended Data Fig. 3)^{17,18}.

To provide further support to the hypothesis that secondary nucleation generates most species responsible for membrane permeation, we performed a set of additional experiments, where the rate of secondary nucleation was modulated by removing fibrils during aggregation through centrifugation (Methods). Specifically, an aggregation reaction starting with $2 \mu\text{M}$ A β 42 (lag time close to 1 h) was stopped after 40 min. The aggregation mixture was then centrifuged for 15 min to remove fibrils and reduce secondary nucleation. We also performed a control experiment where the aggregation was stopped at 40 min and restarted at 60 min without any centrifugation. In both cases, membrane permeation was measured at 2 h.

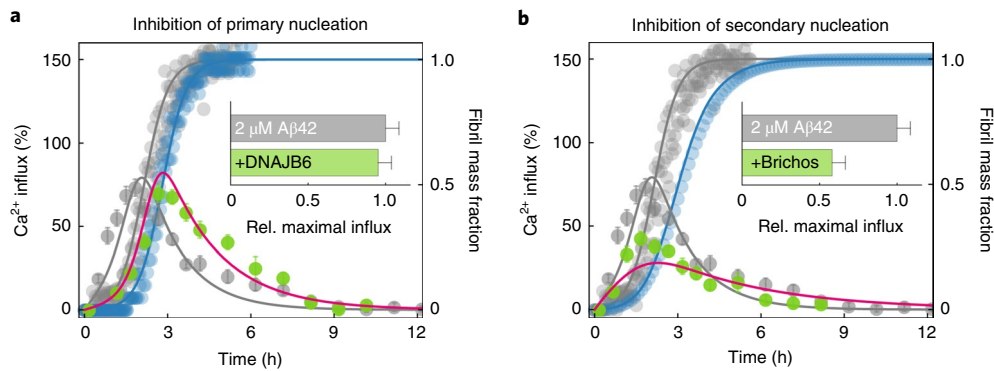


Fig. 3 | Molecular chaperones modulate lipid bilayer permeation induced by the aggregation of A β 42. **a,b**, The effects of two different types of molecular chaperone on lipid bilayer permeability were measured, as monomeric A β 42 was incubated at a concentration of 2 μ M under quiescent conditions in the presence of DNAJB6 (**a**) (0.01% molar equivalents to monomeric A β 42) or Brichos (**b**) (10% molar equivalents to monomeric A β 42). The plots show both the time evolution of amyloid fibril formation and of Ca $^{2+}$ influx in the absence and presence of the respective chaperone. We first fitted our measurements of fibril mass formation to the analytical expression for the aggregation time course (Supplementary Note 1, equation (2)) to determine how the effective rates of primary and secondary nucleation are affected by the chaperones (solid lines). The rate parameters extracted from the analysis (Supplementary Table 3) were then implemented in the analytical expression for the concentration of secondary oligomers (Supplementary Note 1, equations (4–6)) to predict the modulation of lipid bilayer permeability (solid lines). Except for the reduction of the rates of primary and secondary nucleation, the parameters used for calculating the theoretical curves for Ca $^{2+}$ influx were the same as in Fig. 1c. The data in **a** and **b** agree with a model in which membrane permeation correlates with the levels of oligomers generated by secondary nucleation. Indeed, in such a model, inhibiting primary nucleation using DNAJB6 delays the build-up but does not substantially reduce the total concentration of oligomers. Inhibiting secondary nucleation using Brichos, however, reduces the total level of oligomers substantially. The bar charts show the relative maximal extent of Ca $^{2+}$ influx induced by the aggregation of 2 μ M A β 42 in the absence and presence of DNAJB6 and Brichos, respectively. Error bars indicate s.e.m. over three experiments with independent samples.

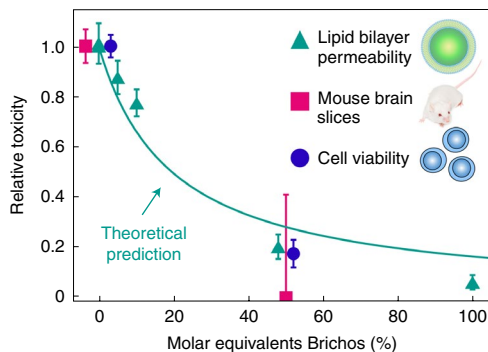


Fig. 4 | Common role of secondary A β 42 oligomers in generating aggregation-associated damage in different systems. The presence of increasing concentrations of Brichos reduces the experimentally measured maximal levels of lipid bilayer permeability (green triangles). These measurements are consistent with the theoretical prediction of the reduction of A β 42 oligomers generated by secondary nucleation (solid line, see Supplementary Note 1, equation (11)). Error bars indicate s.e.m. over three experiments with independent samples. Moreover, the reduction in lipid bilayer permeability in the presence of 50% molar equivalents of Brichos correlates broadly with the observed reduction of the viability of cells in culture (blue circles) and the reduced loss in gamma oscillation in mouse brain slices (pink squares). The cell and mouse brain slice data are taken from ref. ³⁰.

We found that membrane permeation is substantially reduced when the mixture is centrifuged, but there is no substantial change when aggregation is only interrupted (Fig. 1d). This result is in line with the prediction that this protocol would substantially diminish the observed membrane permeation from secondary oligomers, which are now present at lower concentrations, but leave the toxicity from primary oligomers largely unaffected.

The best global fit of the permeation data to the secondary oligomer model yields an exponent $\gamma \approx 1.0 \pm 0.1$ (Fig. 2a). This finding

indicates that the time course of Ca $^{2+}$ influx correlates with the concentration of secondary oligomers, suggesting that membrane permeation is a first-order reaction with respect to the population of secondary oligomers and is thus independent of interactions between oligomers (Fig. 2b and Extended Data Fig. 4a).

We next investigated the question of whether the secondary oligomers are able to exert their damaging effects directly on their formation or if they have first to convert into species that are distinct from those that propagate the aggregation reaction and which possess more specific deleterious activity (lethal oligomers) analogous to events described for prion diseases²⁹. To this end we considered a scenario in which oligomers generated initially through secondary nucleation were assumed not to be toxic but to induce bilayer permeation only after a conversion step to such lethal oligomers over timescales comparable to, or longer than, that of the overall aggregation process (Supplementary Note 1, equation (9)). The comparison between the model predictions and the experimental time course of membrane permeation shows, however, that this model is not able to capture the kinetics of the observed behavior (Fig. 2c,d and Extended Data Fig. 4b), indicating that the oligomers generated on the surfaces of fibrils drive membrane permeation without the need for a structural reorganization that is slow relative to the overall aggregation process. As such, this finding establishes a direct connection between the process of amyloid fibril formation and the toxic effects associated with protein oligomers.

Molecular chaperones modulate lipid bilayer permeation by A β 42 aggregation. We then carried out a series of additional experiments in which the rates of key microscopic steps in the A β 42 aggregation mechanism were modulated selectively by molecular chaperones^{30,31} (Fig. 3) to test further the conclusion that secondary oligomers are correlated with lipid bilayer permeation. We performed experiments in the presence of the chaperone DNAJB6 (0.01% molar equivalents to monomeric A β 42), which at this concentration has been shown to inhibit mainly primary nucleation³¹ (Extended Data Fig. 5), and the Brichos domain (10% molar equivalents to monomeric A β 42) that has been shown to suppress

secondary nucleation³⁰ (Extended Data Fig. 6). The experiments were performed at low concentrations of the chaperones in order still to be able to detect a measurable degree of Ca²⁺ influx, as these chaperones are able to inhibit very effectively the levels of oligomers generated by nucleation processes. In each case, we recorded the effect of each chaperone on the total aggregate mass concentration, as well as on the extent of Ca²⁺ influx (Fig. 3).

The alterations of the rate constants for primary and secondary nucleation in the presence of the chaperones were determined by fitting the aggregate mass measurements to the analytical expression for the time course of amyloid fibril formation (Supplementary Note 1, equation (2), and Supplementary Table 3). These rate parameters were then used to simulate the effects of the chaperones on the population of secondary oligomers over time (Supplementary Note 1, equations (4–6), solid lines). In the presence of DNAJB6 (Fig. 3a), we observed a retardation of membrane permeation that is in agreement with the reduction of the rate of primary nucleation as shown by the theoretical prediction (solid line). In the presence of Brichos, the rate and total extent of Ca²⁺ influx were observed to be reduced, in agreement with the theoretical prediction for the inhibition of secondary nucleation (Fig. 3b). Moreover, turning off secondary nucleation increases the relative importance of oligomers generated by primary nucleation shifting the predicted peak of Ca²⁺ influx to earlier times, in agreement with the experiments. We also studied the effect on membrane permeation of a mutational variant of DNAJB6, S/T18A (Methods). S/T18A has been found to leave the overall aggregation reaction of A β 42 unchanged (Extended Data Fig. 7a)³¹, and indeed, we find here that S/T18A has no detectable effect on the extent of Ca²⁺ influx (Extended Data Fig. 7b). Overall, therefore, the results of this study demonstrate that the oligomers generated by secondary nucleation during the aggregation of A β 42 are the main species responsible, at least in vitro, for disrupting lipid bilayers and permitting an influx of Ca²⁺ ions into vesicles.

Secondary A β 42 oligomers in different systems. Finally, we sought to investigate whether or not the predictions from our model would also allow us to rationalize the role of secondary oligomers in driving toxicity in cellular and animal models (Fig. 4). To this end, we compared our lipid bilayer permeation data with the reduction of viability of cells in culture and with the reduction of gamma oscillations in mouse brain slices, each representing a different readout of the toxic effects of aggregation in vivo³⁰. In particular, we measured the maximal extent of lipid bilayer permeation in the presence of increasing concentrations of Brichos to reduce the rate of secondary nucleation and hence to reduce the production of secondary A β 42 oligomers. We then used our theoretical model (Supplementary Note 1, equation (11), and Extended Data Fig. 8) to predict quantitatively the concentrations of secondary oligomers in the presence of different concentrations of Brichos.

The resulting solid line in Fig. 4 is able to capture the experimentally measured extent of bilayer permeation in vitro. In addition, however, the reduction in the degree of membrane disruption in the presence of Brichos correlates qualitatively with our previous in vivo experimental measurements of cell death and the impairment of gamma oscillations in mouse brain slices³⁰ (Fig. 4).

Discussion

Overall, our results indicate a dominant deleterious role of secondary oligomers resulting from the aggregation of A β 42 in vitro and in vivo. While it is likely that there are additional and more specific mechanisms of toxicity in vivo, such as interactions with receptors and other cellular components^{1–5,32}, our study indicates that the A β 42 oligomers are able to cause lipid membrane disruption, which is directly linked to cellular damage^{19,20}. In this context, a variety of results obtained previously can be rationalized in terms of secondary

oligomers populated during the aggregation process, since their generation requires the presence of both monomeric and fibrillar forms of the protein. Thus, for example, the presence of seed fibrils in addition to monomeric protein in animal models has been found to induce the formation of aggregates of A β 42 associated with neurotoxicity in the brain³³. In addition, the concentration-dependent induction of A β aggregation, and its associated detrimental effects in model organisms on administration of pathological brain extracts³⁴, correlate with the observations from in vitro studies.

In conclusion, our study links directly the generation of secondary oligomers in the presence of monomeric and fibrillar forms of A β 42, to the disruption of lipid membranes. These results, therefore, show directly that aggregation of the A β 42 peptide is specifically linked to the evolution of membrane disruption that gives rise to the type of cellular damage that has been linked to Alzheimer's disease.

Online content

Any methods, additional references, Nature Research reporting summaries, source data, extended data, supplementary information, acknowledgements, peer review information; details of author contributions and competing interests; and statements of data and code availability are available at <https://doi.org/10.1038/s41594-020-0471-z>.

Received: 16 August 2019; Accepted: 25 June 2020;

Published online: 10 August 2020

References

- Dobson, C. M. Protein folding and misfolding. *Nature* **426**, 884–890 (2003).
- Haass, C. & Selkoe, D. J. Soluble protein oligomers in neurodegeneration: lessons from the Alzheimer's amyloid beta-peptide. *Nat. Rev. Mol. Cell Biol.* **8**, 101–112 (2007).
- De Strooper, B. & Karran, E. The cellular phase of Alzheimer's disease. *Cell* **164**, 603–615 (2016).
- Knowles, T. P. J., Vendruscolo, M. & Dobson, C. M. The amyloid state and its association with protein misfolding diseases. *Nat. Rev. Mol. Cell Biol.* **15**, 384–396 (2014).
- Chiti, F. & Dobson, C. M. Protein misfolding, functional amyloid, and human disease: a summary of progress over the last decade. *Annu. Rev. Biochem.* **86**, 27 (2017).
- Campioni, S. et al. A causative link between the structure of aberrant protein oligomers and their toxicity. *Nat. Chem. Biol.* **6**, 140–147 (2010).
- Cremades, N. et al. Direct observation of the interconversion of normal and toxic forms of α -synuclein. *Cell* **149**, 1048–1059 (2012).
- Jucker, M. & Walker, L. C. Self-propagation of pathogenic protein aggregates in neurodegenerative diseases. *Nature* **501**, 45–51 (2013).
- Jaunmuktane, Z. et al. Evidence for human transmission of amyloid- β pathology and cerebral amyloid angiopathy. *Nature* **525**, 247–250 (2015).
- Fusco, G. et al. Structural basis of membrane disruption and cellular toxicity by α -synuclein oligomers. *Science* **358**, 1440–1443 (2017).
- Fitzpatrick, A. W. P. et al. Cryo-EM structures of tau filaments from Alzheimer's disease. *Nature* **547**, 185–190 (2017).
- Qiang, W., Yau, W.-M., Lu, J.-X., Collinge, J. & Tycko, R. Structural variation in amyloid- β fibrils from Alzheimer's disease clinical subtypes. *Nature* **541**, 217–221 (2017).
- Peng, C. et al. Cellular milieu imparts distinct pathological α -synuclein strains in α -synucleinopathies. *Nature* **557**, 558–563 (2018).
- Spillantini, M. G. et al. α -Synuclein in Lewy bodies. *Nature* **388**, 839–840 (1997).
- Knowles, T. P. J. et al. An analytical solution to the kinetics of breakable filament assembly. *Science* **326**, 1533–1537 (2009).
- Michaels, T. C. T. et al. Chemical kinetics for bridging molecular mechanisms and macroscopic measurements of amyloid fibril formation. *Annu. Rev. Phys. Chem.* **69**, 273–298 (2018).
- Cohen, S. I. A. et al. Proliferation of amyloid- β 42 aggregates occurs through a secondary nucleation mechanism. *Proc. Natl Acad. Sci. USA* **110**, 9758–9763 (2013).
- Törnquist, M. et al. Secondary nucleation in amyloid formation. *Chem. Comm.* **54**, 8667–8684 (2018).
- Stefani, M. & Dobson, C. M. Protein aggregation and aggregate toxicity: new insights into protein folding, misfolding diseases and biological evolution. *J. Mol. Med.* **81**, 678–699 (2003).

20. Demuro, A. et al. Calcium dysregulation and membrane disruption as a ubiquitous neurotoxic mechanism of soluble amyloid oligomers. *J. Biol. Chem.* **280**, 17294–17300 (2005).
21. Bode, D. C., Freeley, M., Nield, J., Palma, M. & Viles, J. H. Amyloid- β oligomers have a profound detergent-like effect on lipid membrane bilayers, imaged by atomic force and electron microscopy. *J. Biol. Chem.* **294**, 7566–7572 (2019).
22. Panza, F., Lozupone, M., Loogrosco & Imbimbo, B. P. A critical appraisal of amyloid- β -targeting therapies for Alzheimer disease. *Nat. Rev. Neurol.* **15**, 73–88 (2019).
23. Linse, S. et al. Kinetic fingerprint of antibody therapies predicts outcomes of Alzheimer clinical trials. Preprint at *bioRxiv* <https://doi.org/10.1101/815308> (2019).
24. Sevigny, J. et al. The antibody aducanumab reduces A β plaques in Alzheimer's disease. *Nature* **537**, 50–56 (2016).
25. Walsh, D. M. et al. A facile method for expression and purification of the Alzheimer's disease-associated amyloid β -peptide. *FEBS J.* **276**, 1266–1281 (2009).
26. Flagmeier, P. et al. Ultrasensitive measurement of Ca²⁺ influx into lipid vesicles induced by protein aggregates. *Angew. Chem. Int. Ed.* **56**, 7750–7754 (2017).
27. Michaels, T. C. T. et al. Dynamics of oligomer populations formed during the aggregation of Alzheimer's A β 42 peptide. *Nat. Chem.* **12**, 445–451 (2020).
28. Hellstrand, E., Boland, B., Walsh, D. M. & Linse, S. Amyloid β -protein aggregation produces highly reproducible kinetic data and occurs by a two-phase process. *ACS Chem. Neurosci.* **1**, 13–18 (2010).
29. Sandberg, M. K., Al-Doujaily, H., Sharps, B., Clarke, A. R. & Collinge, J. Prion propagation and toxicity in vivo occur in two distinct mechanistic phases. *Nature* **470**, 540–542 (2011).
30. Cohen, S. I. A. et al. A molecular chaperone breaks the catalytic cycle that generates toxic A β oligomers. *Nat. Struct. Mol. Biol.* **22**, 207–213 (2015).
31. Mansson, C. et al. Interaction of the molecular chaperone DNAJB6 with growing amyloid-beta 42 (A β 42) aggregates leads to sub-stoichiometric inhibition of amyloid formation. *J. Biol. Chem.* **289**, 31066–31076 (2014).
32. Dunning, C. J. et al. Direct high affinity interaction between A β 42 and GSK3 α stimulates hyperphosphorylation of tau. A new molecular link in Alzheimer's disease? *ACS Chem. Neurosci.* **7**, 161–170 (2016).
33. Sowade, R. F. & Jahn, T. R. Seed-induced acceleration of amyloid- β mediated neurotoxicity in vivo. *Nat. Commun.* **8**, 512 (2017).
34. Eisele, Y. S. et al. Peripherally applied A β -containing inoculates induce cerebral β -amyloidosis. *Science* **330**, 980–982 (2010).

Publisher's note Springer Nature remains neutral with regard to jurisdictional claims in published maps and institutional affiliations.

© The Author(s), under exclusive licence to Springer Nature America, Inc. 2020

Methods

Preparation and purification of recombinant A β 42. The recombinant A β 42 (M1-42) peptide (MDAEFRHDSGYEVHHQKLVFF AEDVGSNKGAIIGLMVGGVVIA), here called A β 42, was expressed in the *Escherichia coli* BL21 Gold (DE3) strain and purified as described previously with slight modifications^{25,35}.

Preparation of recombinant A β 42 for kinetic experiments. Solutions of monomeric recombinant A β 42 were prepared as previously described by dissolving the lyophilized A β 42 peptide in 6 M of GuHCl then purifying the protein using a Superdex 75 10/300 GL column (GE Healthcare Bio-Sciences AB SE-751 84). The center of the elution peak was collected, and the peptide concentration was determined from the absorbance of the integrated peak area using $\epsilon_{280} = 1,4901 \text{ mol}^{-1} \text{ cm}^{-1}$.

Measurement of aggregation kinetics of A β 42. For kinetic experiments the A β 42 monomer was diluted with buffer and supplemented with 20 μM ThT. All samples were prepared in low-binding Eppendorf tubes (Eppendorf) on ice. Each sample was then pipetted into multiple wells of a 96-well half area, low-binding polyethylene glycol coating plate (Corning 3881) with a clear bottom, at 80 μl per well. The 96-well plate was placed in a plate reader (Fluostar Omega, Fluostar Optima or Fluostar Galaxy; BMG Labtech) and incubated at 37 °C under quiescent conditions using the bottom reading mode (440-nm excitation filter, 480-nm emission filter). For each new preparation of protein, the aggregation kinetics were checked by performing reactions at different concentrations of A β 42.

A β 42 aggregation. A β 42 aggregation reactions were performed in 20 mM of sodium phosphate buffer, pH 8, supplemented with 20 μM of ThT and 200 μM of EDTA. Samples were prepared in low-binding Eppendorf tubes on ice by avoiding any introduction of air bubbles. All aggregation reactions were performed in a 96-well half area, low-binding, clear-bottom polyethylene glycol- (PEG-) coated plate (Corning 3881). Plates were sealed to prevent any evaporation. Aggregation assays were performed at 37 °C under quiescent conditions. Aliquots for measurements of Ca²⁺ influx were then taken into low-binding tubes at the desired times after the plate was placed in the incubator.

Seeded aggregation. Preformed fibrils of A β 42, which are used as seed, were prepared just before the experiment. Fibrils were prepared by aggregating 4 μM of A β 42 overnight in 20 mM of sodium phosphate, 200 μM of EDTA, pH 8.0 and 20 μM of ThT. ThT fluorescence was monitored over time to ensure that the fibrils were formed. Then samples were collected from the wells into low-binding Eppendorf tubes and sonicated for 2 min in a sonicator bath at room temperature. Under this condition, the final concentration of fibrils (4 μM of A β 42) was considered to be equal to the initial concentration of the monomer, as there was negligible presence of free monomer left in solution. Preformed A β 42 fibrils (2.5%) were subsequently added to the 2 μM of freshly prepared monomer solution to perform seeded aggregation. This aggregation reaction was also performed in 20 mM of sodium phosphate, 20 μM of ThT and 200 μM of EDTA at pH 8.0 at 37 °C under quiescent conditions.

Preparation and purification of the Brichos domain. proSP-C Brichos was expressed in *E. coli* and purified as described previously³⁶.

Preparation and purification of the chaperone DNAJB6 and its mutational variant S/T18A. Human DNAJB6b (isoform b, UniProt ID O75190-2) with a hexa-His tag was expressed recombinantly in *E. coli* ER2566 and purified as described previously³⁷ but with an additional washing step using 8 M of urea during the affinity chromatography to remove bound bacterial proteins³⁷. Just before its use, DNAJB6 was dialyzed into the assay buffer (20 mM of sodium phosphate buffer at pH 8, 0.2 mM of EDTA and 0.02% sodium azide) using Slide-A-Lyser MINI (Thermo Scientific).

Preparation and purification of dye filled vesicles. The dye filled vesicles were prepared as previously described²⁶. Phospholipids 16:0-18:1 PC (catalog no. 850457) and biotinylated lipids 18:1-12:0 Biotin PC (catalog no. 860563) were purchased from Avanti Polar Lipids in the form of powder and chloroform solutions, respectively. Chloroform stock solutions were mixed such that the ratio between 16:0-18:1 PC and 18:1-12:0 biotin PC was 100:1, and the chloroform was then removed under vacuum in a desiccator overnight. The samples were then dissolved in HEPES buffer (pH 6.5) with 100 μM of Cal-520 and five freeze-and-thaw cycles were performed using dry ice and a water bath. The solution was passed at least ten times through an extruder (Avanti Polar Lipids) with a membrane of an appropriate size cut off of 200 μm . The size of the vesicles was determined using a Zetasizer (Zetasizer Nano ZSP, Malvern Instruments). To separate nonincorporated dye molecules from the solution surrounding the vesicles, size-exclusion chromatography was performed²⁶.

Preparation of PEGylated slides and immobilization of single vesicles. We followed the previously described protocol for slide preparation to perform

the membrane permeabilization assay²⁶. Borosilicate glass coverslides (VWR International, 22 \times 22 mm², product no. 63 1-0122) were cleaned by subsequent sonication in 2% (v/v) Hellmanex III (Hellma) in milliQ water, twice in milliQ water, methanol and again in water for 10 min each. The glass slides were dried under a nitrogen stream, and plasma-etched using an argon plasma cleaner (PDC-002, Harrick Plasma) for 20 min before Frame-Seal incubation chambers (9 \times 9 mm², Biorad, product number SLF-0601) were affixed to the glass slides. Then 50 μl of a mixture of 100:1 PLL-g-PEG (SuSoS) and PLL-g-PEG biotin (SuSoS) (1 g l⁻¹) in reaction buffer (50 mM of HEPES, pH 6.5) was added to the coverslide inside of the chamber and incubated for 30 min. The coverslides were washed three times with filtered reaction buffer. Next, 50 μl of a solution of 0.1 mg ml⁻¹ of Neutravidin (Thermo Scientific) in reaction buffer was added to the coverslide and incubated for 15 min, and washed three times with reaction buffer. Finally, 50 μl of the solution of purified vesicles was added to the coverslide and incubated for 30 min before washing carefully at least five times with reaction buffer.

Imaging using total internal reflection fluorescence microscope (TIRFM). Imaging was performed using a homebuilt TIRFM based on an inverted Olympus IX-71 microscope as previously described in detail²⁶. A 488-nm laser (Toptica, iBeam smart, 200 mW) was used to excite the sample. The expanded and collimated laser beam was focused using two Plano-convex lens onto the back-focal plane of the $\times 60$, 1.49 numerical aperture oil immersion objective lens (APON60XO TIRF, Olympus, product no. N2709400) to a spot of adjustable diameter. The fluorescence signal was collected by the same objective and was separated from the excitation beam by a dichroic laser (Di01-R405/488/561/635, Semrock). The emitted light was passed through an appropriate set of filters (BLP01-488R, Semrock and FF01-520/44-25, Semrock). The fluorescence signal was then passed through a 2.5 \times beam expander and imaged onto a 512 \times 512 pixel EMCCD camera (Photometrics Evolve, E VO-512-M-FW-16-AC-110). Images were acquired with a 488-nm laser (10 W cm⁻²) for 50 frames with a scan speed of 20 Hz and bit depth of 16 bits. Each pixel corresponds to 100 nm. All the measurements were carried out under ambient conditions ($T = 295 \text{ K}$). The open source microscopy manager software Micro Manager 1.4 was used to control the microscope hardware and image acquisition.

Performing the Ca²⁺ influx assay using TIRFM. The imaging of the induced membrane permeability was performed as previously described²⁶. Single vesicles tethered to PLL-PEG coated borosilicate glass coverslides (VWR International, 22 \times 22 mm², product number 63 1-0122) were placed on an oil immersion objective mounted on an inverted Olympus IX-71 microscope. Each coverslide was affixed to Frame-Seal incubation chambers and was incubated with 50 μl of HEPES buffer at pH 6.5. Just before the imaging, the HEPES buffer was replaced with 50 μl of Ca²⁺ containing buffer solution L-15. Then, 16 (4 \times 4) images of the coverslide were recorded under three different conditions (background, in the presence of A β 42 and after addition of ionomycin (Cambridge Bioscience), respectively). The distance between each field of view was set to 100 μm , and was automated (bean-shell script, Micro Manager) to avoid any user bias. After each measurement the script allowed the stage (PRIOR H117) to move the field of view back to the start position such that identical fields of view could be acquired for the three different conditions.

Data analysis to quantify the extent of Ca²⁺ influx. The fluorescence intensity of individual vesicles was determined as previously described²⁶. The recorded images were analyzed using ImageJ to determine the fluorescence intensity of each spot under the three different conditions, namely background ($F_{\text{background}}$), in the presence of an aggregation mixture ($F_{\text{aggregate}}$) and after the addition of ionomycin ($F_{\text{ionomycin}}$). The relative influx of Ca²⁺ into an individual vesicle due to aggregates of A β 42 peptide was then determined using the following equation:

$$\text{Ca}^{2+} \text{ influx} = \Phi = \frac{F_{\text{aggregate}} - F_{\text{background}}}{F_{\text{ionomycin}} - F_{\text{background}}}$$

The average degree of Ca²⁺ influx was calculated by averaging the Ca²⁺ influx into individual vesicles.

Fibril spin-down experiment. To check whether the oligomers formed during secondary nucleation are the main source of species causing membrane permeabilization, we performed an aggregation where the rate of secondary nucleation was substantially reduced by removing insoluble fibrils from the aggregation reaction. We aggregated 2 μM of A β 42 in 20 mM of sodium phosphate buffer at pH 8, mixed with 20 μM of ThT and 200 μM of EDTA for 40 min in clear-bottom 96-well plates (lag phase, $\sim 1 \text{ h}$) and then arrested the aggregation by putting it to the ice bath. Immediately, we transferred the aggregation mixture into a low-binding Eppendorf and centrifuged for 15 min at 4 °C to remove as many fibrils as possible. Then we transferred the supernatant back into clear-bottom 96-well plates for 60 min at 37 °C and followed the aggregation. We also performed a control experiment where the aggregation was stopped at 40 min using ice bath and the aggregation restarted at 60 min at 37 °C without any centrifugation.

Reporting Summary. Further information on research design is available in the Nature Research Reporting Summary linked to this article.

Data availability

The authors confirm that all data generated and analyzed during this study are included in this published article and its Supplementary Information. Source data are provided with this paper.

Code availability

All simulation and data analysis codes are included in this article and its Supplementary Information. Codes are available from the corresponding authors on request.

References

35. Habchi, J. et al. Systematic development of small molecules to inhibit specific microscopic steps of A β 42 aggregation in Alzheimer's disease. *Proc. Natl Acad. Sci. USA* **114**, E200–E208 (2017).
36. Willander, H. et al. High-resolution structure of a BRICHOS domain and its implications for anti-amyloid chaperone activity on lung surfactant protein C. *Proc. Natl Acad. Sci. USA* **109**, 2325–2329 (2012).
37. Blennow, A., Surin, B. P., Ehring, H., Mc Lennan, N. F. & Spangfort, M. D. Isolation and biochemical characterization of highly purified *Escherichia coli* molecular chaperone Cpn60 (GroEL) by affinity chromatography and urea-induced monomerization. *Biochim. Biophys. Acta* **1252**, 69–78 (1995).

Acknowledgements

This study has been supported by the Boehringer Ingelheim Fonds (P.F.), the German National Merit Foundation (P.F.), a Marie-Curie Individual Fellowship (S.D.), Peterhouse,

Cambridge (T.C.T.M.), the Swiss National Science Foundation (T.C.T.M.), the Wellcome Trust (T.P.J.K., C.M.D., M.V.), the Swedish Research Council (S.L.), the Royal Society (D.K.), the Frances and Augustus Newman Foundation (T.P.J.K.), the Biotechnology and Biological Sciences Research Council (T.P.J.K.) and the Cambridge Centre for Misfolding Diseases (P.F., T.P.J.K., M.V. and C.M.D.).

Author contributions

P.F. and S.D. performed the experiments. T.C.T.M. developed the theoretical model and performed the kinetic analysis. P.F., S.D., T.C.T.M., X.Y., A.J.D., C.E., M.V., S.L., D.K., T.P.J.K. and C.M.D. participated in designing the study, interpreting the results and writing the paper. P.F., S.D. and T.C.T.M. contributed equally to this work.

Competing interests

The authors declare no competing interests.

Additional information

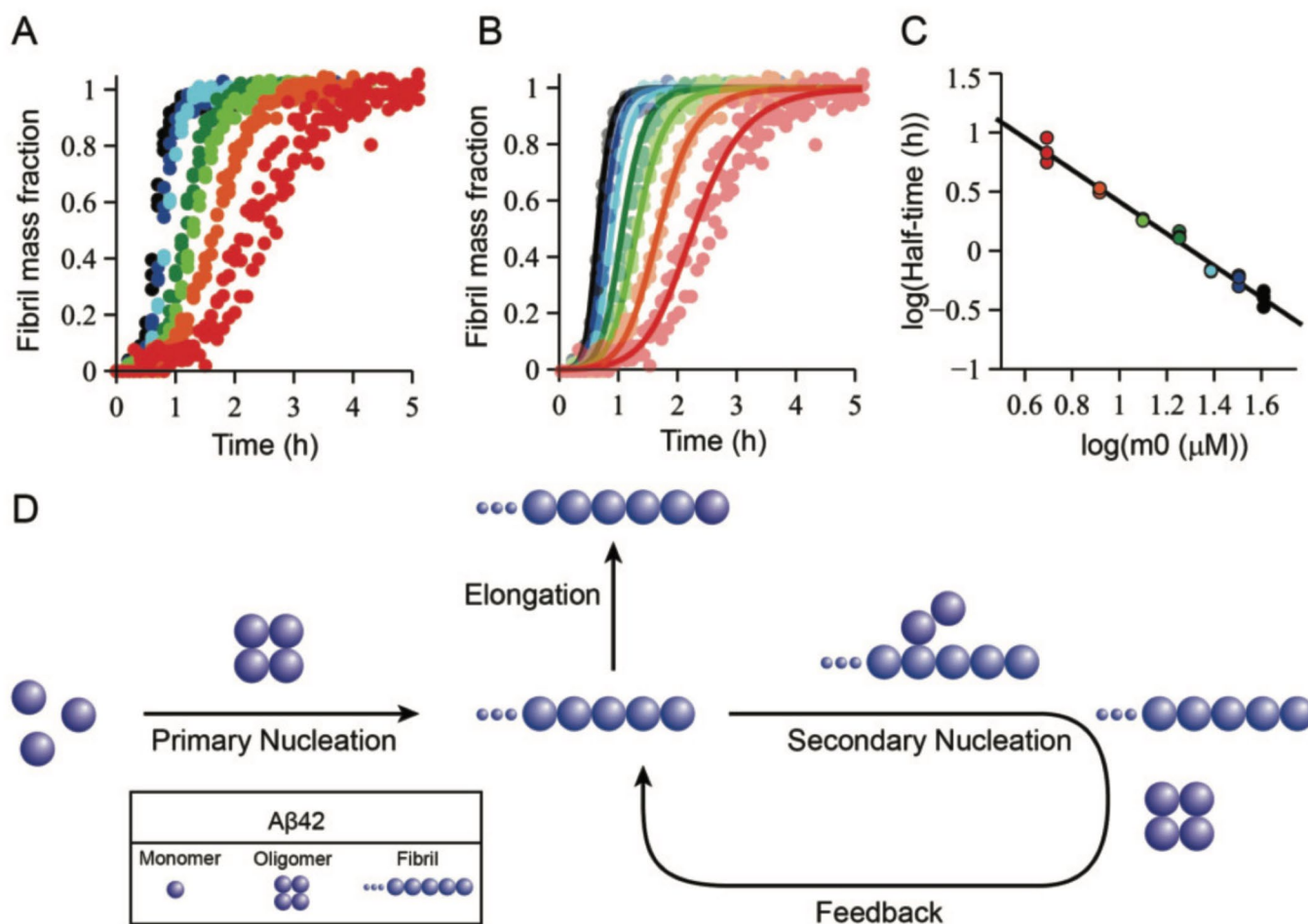
Extended data is available for this paper at <https://doi.org/10.1038/s41594-020-0471-z>.

Supplementary information is available for this paper at <https://doi.org/10.1038/s41594-020-0471-z>.

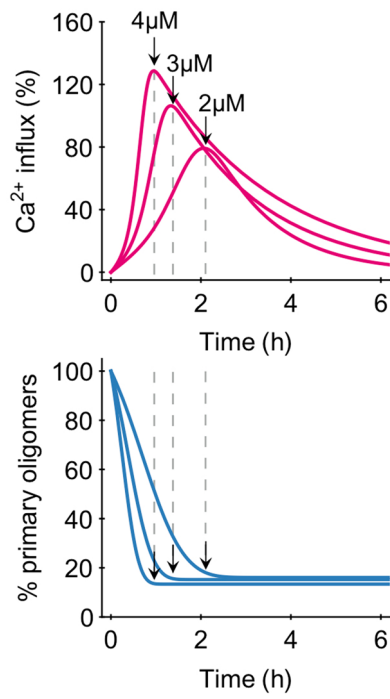
Correspondence and requests for materials should be addressed to D.K. or T.P.J.K.

Peer review information Inés Chen was the primary editor on this article and managed its editorial process and peer review in collaboration with the rest of the editorial team.

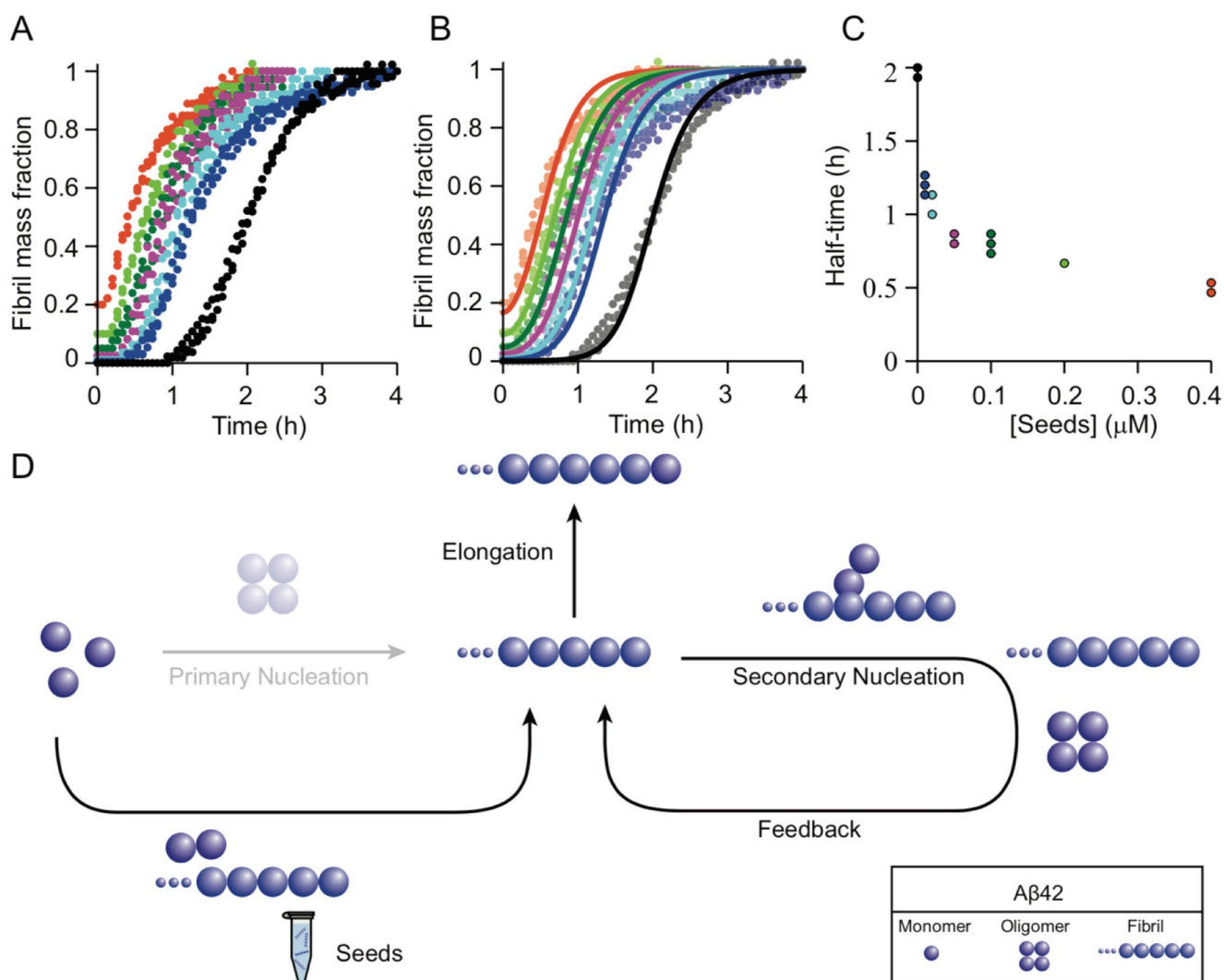
Reprints and permissions information is available at www.nature.com/reprints.



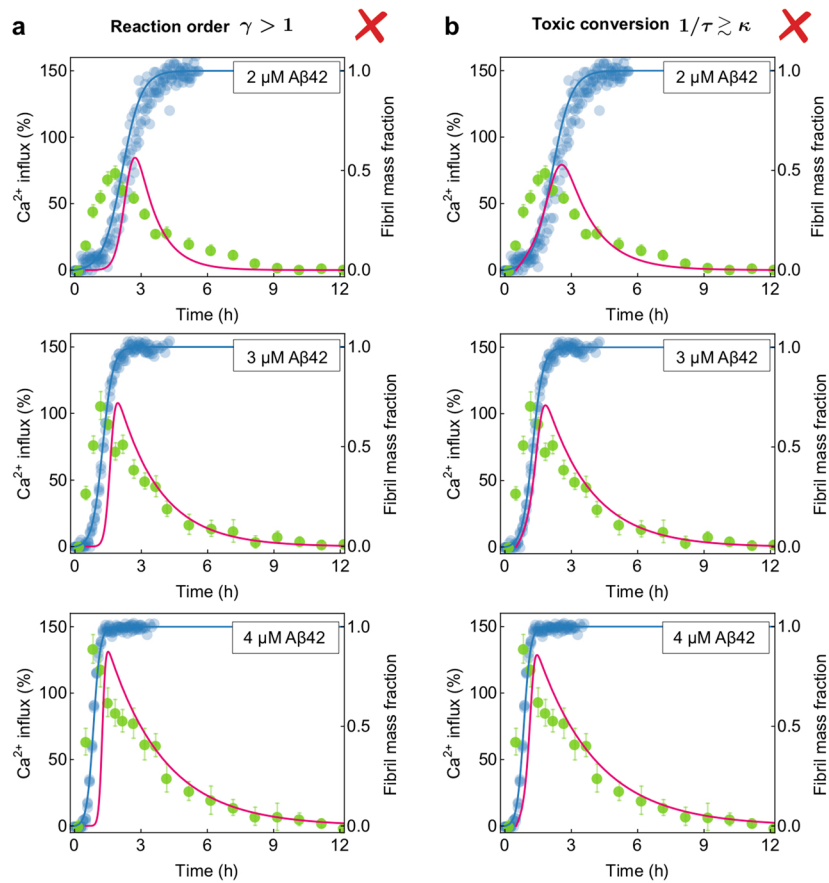
Extended Data Fig. 1 | Reproducible aggregation kinetics of recombinant Aβ42. **a**, Monomeric Aβ42 is incubated in the presence of 20 μM ThT under quiescent conditions at 37 °C (red: 2 μM, orange: 2.5 μM, light green: 3 μM, dark green: 3.5 μM, light blue: 4 μM, dark blue: 4.5 μM, black: 5 μM). **b**, Global fit to the kinetic traces of the Aβ42 aggregation to Supplementary Note 1, Eq. 2, yielding the parameters of Supplementary Table 1. **c**, Half-times of the aggregation reaction. **d**, Drawing of the microscopic events of Aβ42 aggregation. Monomeric protein forms small aggregates (for example oligomers) during primary nucleation and these convert into fibrils and their fibril mass grows via elongation. An autocatalytic process, namely secondary nucleation, that depends on both the monomer and fibril concentration leads to an amplification of the aggregation reaction.



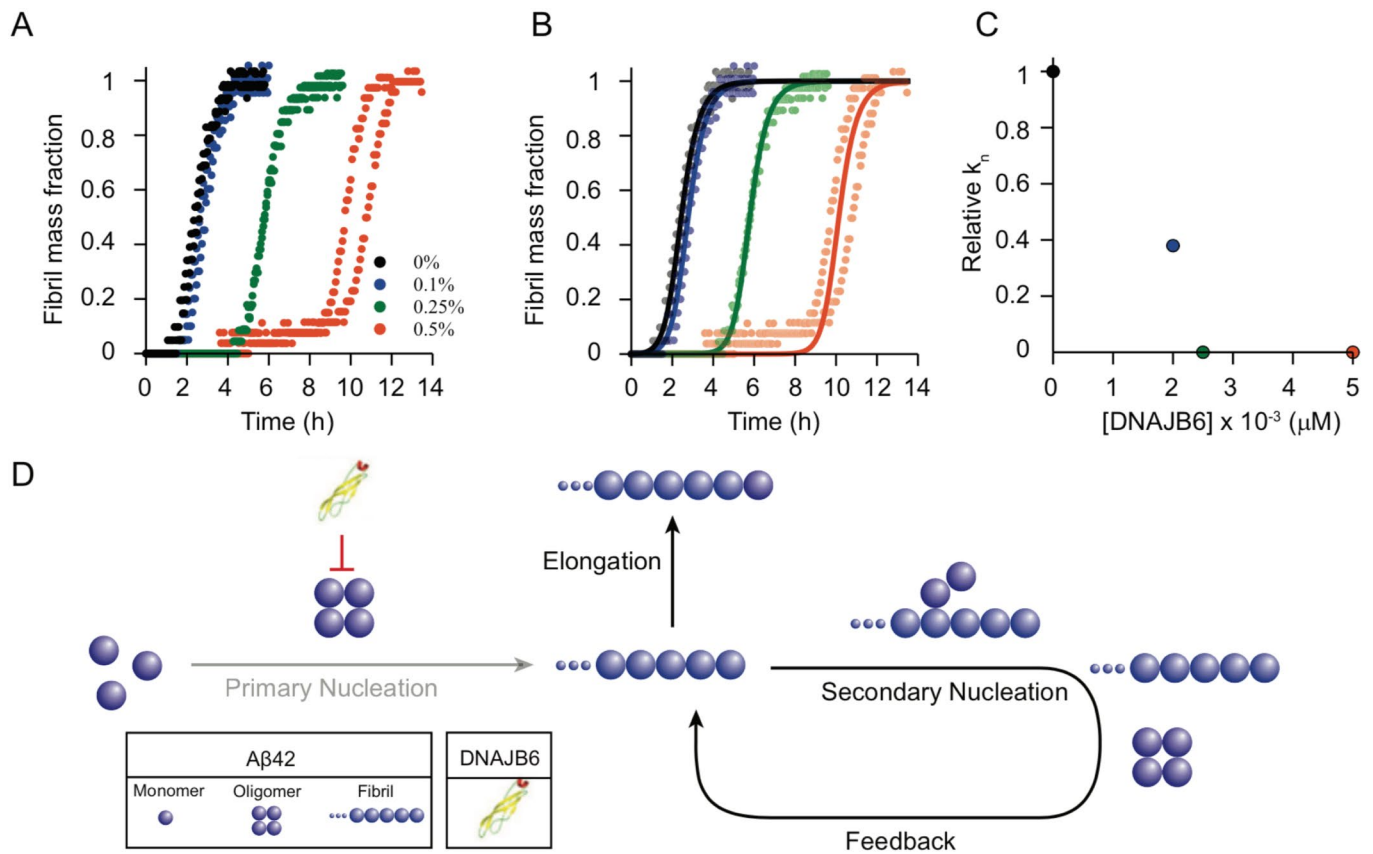
Extended Data Fig. 2 | Oligomer concentrations are dominated by secondary oligomers. Fraction of primary oligomers (over total oligomer population) calculated using the fitting parameters of Fig. 1c of the main text.



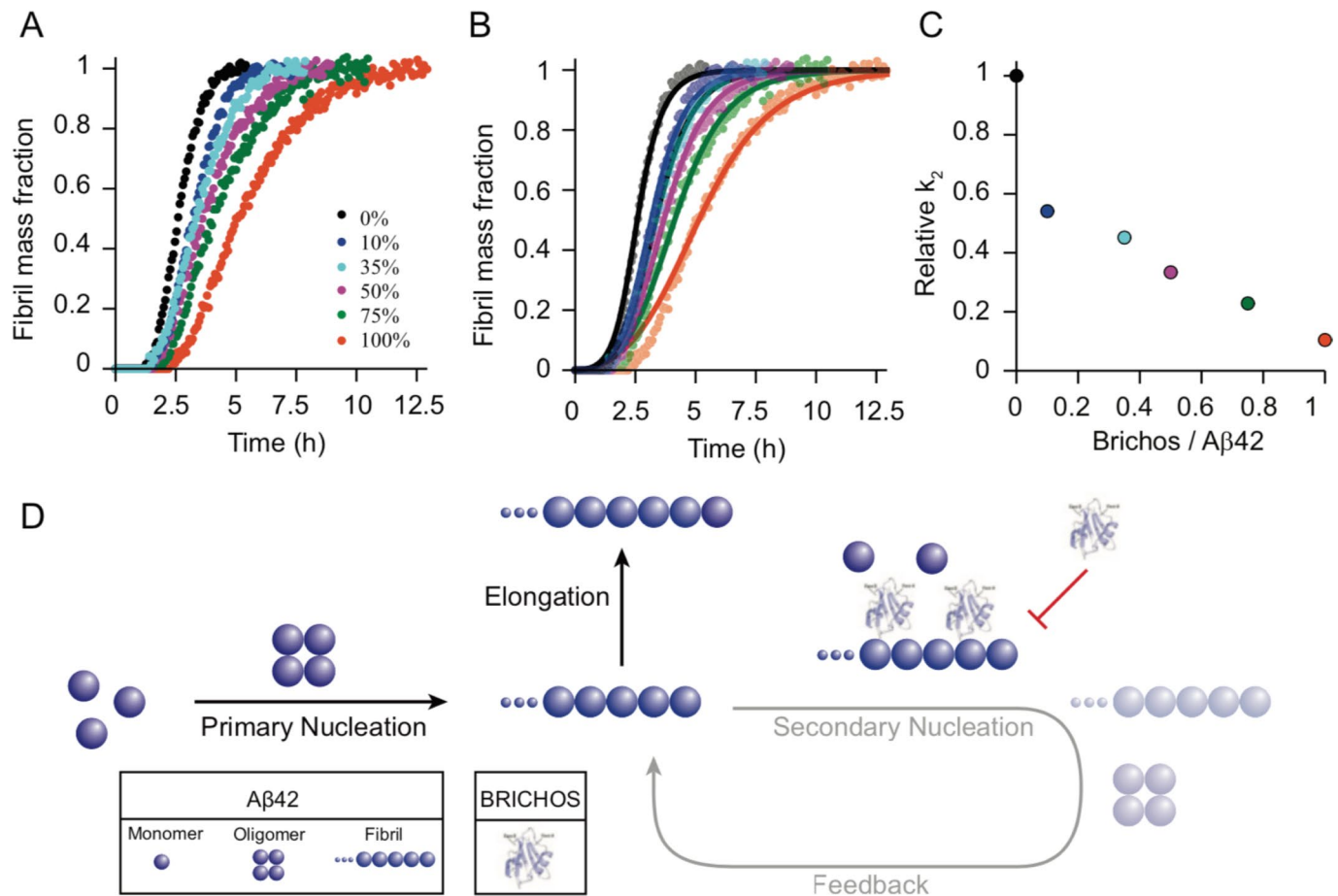
Extended Data Fig. 3 | The addition of seed fibrils accelerates the aggregation of A β 42. **a**, Monomeric A β 42 was incubated at a concentration of 2 μM in the presence of 20 μM ThT at 37 $^{\circ}\text{C}$ under quiescent conditions in the presence of no (red), 0.5% (orange), 1% (light green), 2.5% (dark green), 10% (blue) and 20% (black) preformed fibrils. **b**, Global fits to the kinetic traces of the aggregation reaction. **c**, The half-times of the aggregation reaction with varying concentrations of seed fibrils. **d**, Drawing of the microscopic events of A β 42 aggregation in the presence of the preformed fibrils that accelerate the aggregation. Addition of seed fibrils allows bypassing de novo formation of new aggregates by primary nucleation, favouring secondary nucleation.



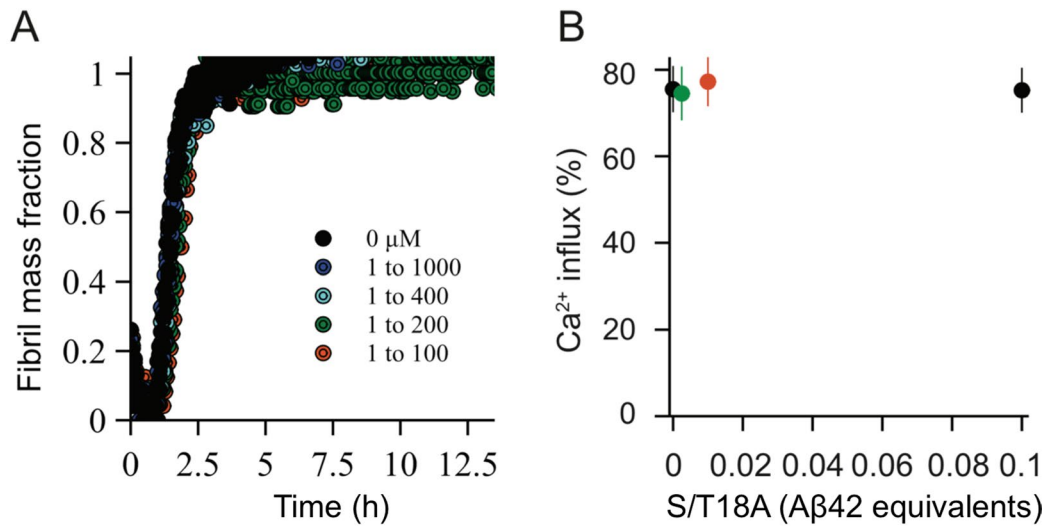
Extended Data Fig. 4 | Role of cooperativity and toxic conversion. **a**, Best global fit of experimental Ca^{2+} -influx data to secondary oligomer kinetic model with reaction order $\gamma = 3$ (Supplementary Note 1, Eq. 8). **b**, Misfit of permeation measurements to a kinetic model that assumes slow toxic conversion of oligomers generated initially through secondary nucleation (Supplementary Note 1, Eq. 9). Theoretical predictions were generated assuming an arbitrary timescale for conversion comparable to that of the aggregation reaction ($\tau = 0.5$ h in this case).



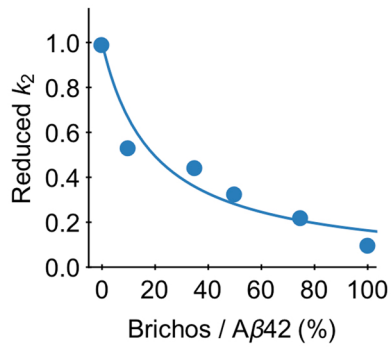
Extended Data Fig. 5 | The chaperone DNAJB6 inhibits primary nucleation of Aβ42 aggregation. **a**, Monomeric Aβ42 was incubated at a concentration of 2 μM in the presence of 20 μM ThT at 37 °C under quiescent conditions in the absence (black) and presence (blue: 0.1%, green: 0.25%, orange: and 0.5% relative to monomeric Aβ42) of DNAJB6. **b**, Global fits to the kinetic traces. **c**, Relative primary nucleation rate k_n . **d**, Drawing of the microscopic events of Aβ42 aggregation in the presence of DNAJB6 that inhibits primary nucleation.



Extended Data Fig. 6 | The BRICHOS domain inhibits secondary nucleation of Aβ42 aggregation and the membrane disruption ability of Aβ42 oligomers. **a**, Monomeric Aβ42 was incubated at a concentration of 2 μM in the presence of 20 μM ThT at 37 °C under quiescent conditions in the absence (black) and presence (dark blue: 10%, cyan: 35%, magenta: 50%, green: 75% and orange 100% relative to monomeric Aβ42) of the Brichos domain. **b**, Fits to the kinetic traces of the aggregation reactions in the presence of the BRICHOS domain to determine its influence on secondary nucleation. **c**, Relative secondary nucleation rate constants k_2 of the aggregation of Aβ42 with increasing concentrations of the BRICHOS domain. **d**, Drawing of the microscopic events of Aβ42 aggregation in the presence of the BRICHOS domain that inhibits secondary nucleation.



Extended Data Fig. 7 | The mutant variant S/T18A of DNAJB6 does neither influence the primary nucleation of Aβ42 nor its ability to disrupt the membrane at the same concentrations. a, Aggregation kinetics of Aβ42 in the presence of the mutant variant S/T18A. **b,** Effect of S/T18A on the ability of aliquots taken at a time point corresponding to maximal Ca²⁺ influx.



Extended Data Fig. 8 | Analysis of relative secondary nucleation rate with increasing BRICHOS concentration. Relative secondary nucleation rate constants k_2 of the aggregation of A β 42 with increasing concentrations of the BRICHOS domain (from Extended Data Fig. 6c) fitted to Supplementary Note 1, Eq. 11 (solid line).

Reporting Summary

Nature Research wishes to improve the reproducibility of the work that we publish. This form provides structure for consistency and transparency in reporting. For further information on Nature Research policies, see [Authors & Referees](#) and the [Editorial Policy Checklist](#).

Statistics

For all statistical analyses, confirm that the following items are present in the figure legend, table legend, main text, or Methods section.

- | | |
|-----|-----------|
| n/a | Confirmed |
|-----|-----------|
- The exact sample size (n) for each experimental group/condition, given as a discrete number and unit of measurement
 - A statement on whether measurements were taken from distinct samples or whether the same sample was measured repeatedly
 - The statistical test(s) used AND whether they are one- or two-sided
Only common tests should be described solely by name; describe more complex techniques in the Methods section.
 - A description of all covariates tested
 - A description of any assumptions or corrections, such as tests of normality and adjustment for multiple comparisons
 - A full description of the statistical parameters including central tendency (e.g. means) or other basic estimates (e.g. regression coefficient) AND variation (e.g. standard deviation) or associated estimates of uncertainty (e.g. confidence intervals)
 - For null hypothesis testing, the test statistic (e.g. F , t , r) with confidence intervals, effect sizes, degrees of freedom and P value noted
Give P values as exact values whenever suitable.
 - For Bayesian analysis, information on the choice of priors and Markov chain Monte Carlo settings
 - For hierarchical and complex designs, identification of the appropriate level for tests and full reporting of outcomes
 - Estimates of effect sizes (e.g. Cohen's d , Pearson's r), indicating how they were calculated

Our web collection on [statistics for biologists](#) contains articles on many of the points above.

Software and code

Policy information about [availability of computer code](#)

Data collection

Imaging data are acquired using an automated program written using bean-shell based script which is implemented in Micro-manager.

Data analysis

Mathematica Version 11; Imaging data were analyzed using Image J and analysed using Origin 9.1

For manuscripts utilizing custom algorithms or software that are central to the research but not yet described in published literature, software must be made available to editors/reviewers. We strongly encourage code deposition in a community repository (e.g. GitHub). See the Nature Research [guidelines for submitting code & software](#) for further information.

Data

Policy information about [availability of data](#)

All manuscripts must include a [data availability statement](#). This statement should provide the following information, where applicable:

- Accession codes, unique identifiers, or web links for publicly available datasets
- A list of figures that have associated raw data
- A description of any restrictions on data availability

The authors confirm that all data generated and analysed during this study are included in this published article (and its supplementary information files).

Field-specific reporting

Please select the one below that is the best fit for your research. If you are not sure, read the appropriate sections before making your selection.

- Life sciences Behavioural & social sciences Ecological, evolutionary & environmental sciences

For a reference copy of the document with all sections, see nature.com/documents/nr-reporting-summary-flat.pdf

Life sciences study design

All studies must disclose on these points even when the disclosure is negative.

Sample size	<input type="text" value="N/A"/>
Data exclusions	<input type="text" value="N/A"/>
Replication	<input type="text" value="All attempts at replication were successful."/>
Randomization	<input type="text" value="N/A"/>
Blinding	<input type="text" value="N/A"/>

Reporting for specific materials, systems and methods

We require information from authors about some types of materials, experimental systems and methods used in many studies. Here, indicate whether each material, system or method listed is relevant to your study. If you are not sure if a list item applies to your research, read the appropriate section before selecting a response.

Materials & experimental systems

n/a	Involvement in the study
<input checked="" type="checkbox"/>	<input type="checkbox"/> Antibodies
<input checked="" type="checkbox"/>	<input type="checkbox"/> Eukaryotic cell lines
<input checked="" type="checkbox"/>	<input type="checkbox"/> Palaeontology
<input checked="" type="checkbox"/>	<input type="checkbox"/> Animals and other organisms
<input checked="" type="checkbox"/>	<input type="checkbox"/> Human research participants
<input checked="" type="checkbox"/>	<input type="checkbox"/> Clinical data

Methods

n/a	Involvement in the study
<input checked="" type="checkbox"/>	<input type="checkbox"/> ChIP-seq
<input checked="" type="checkbox"/>	<input type="checkbox"/> Flow cytometry
<input checked="" type="checkbox"/>	<input type="checkbox"/> MRI-based neuroimaging